



HAL
open science

Total Surface Current Vector and Shear From a Sequence of Satellite Images: Effect of Waves in Opposite Directions

Fabrice Ardhuin, Matias Alday, Maria Yurovskaya

► **To cite this version:**

Fabrice Ardhuin, Matias Alday, Maria Yurovskaya. Total Surface Current Vector and Shear From a Sequence of Satellite Images: Effect of Waves in Opposite Directions. *Journal of Geophysical Research. Oceans*, 2021, 126 (7), 10.1029/2021JC017342 . insu-03439239

HAL Id: insu-03439239

<https://insu.hal.science/insu-03439239>

Submitted on 22 Nov 2021

HAL is a multi-disciplinary open access archive for the deposit and dissemination of scientific research documents, whether they are published or not. The documents may come from teaching and research institutions in France or abroad, or from public or private research centers.

L'archive ouverte pluridisciplinaire **HAL**, est destinée au dépôt et à la diffusion de documents scientifiques de niveau recherche, publiés ou non, émanant des établissements d'enseignement et de recherche français ou étrangers, des laboratoires publics ou privés.

1 **Total Surface Current Vector and Shear from a**
2 **Sequence of Satellite images:**
3 **Effect of Waves in Opposite Directions**

4 **Fabrice Ardhuin^{1,2}and Matias Alday¹**

5 **Maria Yurovskaya^{3,4}**

6 ¹Univ. Brest, CNRS, Ifremer, IRD, Laboratoire d'Océanographie Physique et Spatiale, Brest, France

7 ²Scripps Institution of Oceanography, University of California San Diego, La Jolla, California

8 ³Marine Hydrophysical Institute of RAS, Sevastopol, Russia

9 ⁴Russian State Hydrometeorological Institute, St. Petersburg, Russia

10 **Key Points:**

- 11 • Phase shifts in lagged pairs of satellite images yield information on near surface
12 current and shear
- 13 • Waves in opposite directions can corrupt current estimates in particular for
14 wavelengths under 25 m
- 15 • A sequence of 3 images can allow a separation of waves in opposing direction
16 and a current estimate

Corresponding author: Fabrice Ardhuin, ardhuin@ifremer.fr

Abstract

The Total Surface Current Velocity (TSCV) - the horizontal vector quantity that advects seawater - is an Essential Climate Variable, with few observations available today. The TSCV can be derived from the phase speed of surface gravity waves, and the estimates of the phase speeds of different wavelengths could give a measure of the vertical shear. Here we combine 10-m resolution Level-1C of the Sentinel 2 Multispectral Instrument, acquired with time lags up to 1s, and numerical simulation of these images. Retrieving the near surface shear requires a specific attention to waves in opposing direction when estimating a single phase speed from the phase difference in an image pair. Opposing waves lead to errors in phase speeds that are most frequent for shorter wavelengths. We propose an alternative method using a least-square fit of the current speed and amplitudes of waves in opposing directions to the observed complex amplitudes of a sequence of 3 images. When applied to Sentinel 2, this method generally provides more noisy estimate of the current. A byproduct of this analysis is the "opposition spectrum" that is a key quantity in the sources of microseisms and microbaroms. For future possible sensors, the retrieval of TSCV and shear can benefit from increased time lags, resolution and exposure time of acquisition. These findings should allow new investigations of near-surface ocean processes including regions of freshwater influence or internal waves, using existing satellite missions such as Sentinel 2, and provide a basis for the design of future optical instruments.

Plain Language Summary

Measuring ocean surface current and its vertical variation is important for a wide range of science questions and applications. A well known technique for measuring currents from ocean surface images is to follow the motion of wave crests from one image to another, measuring their celerity. The values obtained for different wavelengths give access to an estimate of the current at different depths. When using only two images, the technique breaks down if there are waves travelling in opposing directions with comparable energy levels. We show that this is generally a problem for shorter wave components because there are generally waves in opposing directions with significant energy for wavelengths shorter than 25 m. Here we generalize the technique to a sequence of 3 images that allows to separate the waves in opposing directions. Applications of this method to existing data from the Sentinel 2 satellite is difficult due to short time differences between image acquisitions. Several improvements on the Sentinel 2 sensor are proposed for a specific instrument that would measure surface current and shear.

1 Introduction

Surface current velocities play an important role in many ocean processes, including the flux of kinetic energy from the atmosphere to the ocean (Wunsch & Ferrari, 2009), air-sea fluxes (Cronin et al., 2019), and the transport of buoyant material (Maximenko et al., 2019). Different observation systems have been proposed to measure the surface current in a wide range of conditions. Barrick (1977) and many others have developed land-based HF radars that rely on the dispersion relation of surface gravity waves, while open ocean conditions are very sparsely monitored by a wide range of techniques that differ in their effective depth of measurement, as illustrated in Fig. 1. In situ moorings are typically limited to measurements at depths larger than 5 m, away from the layer where the Stokes drift of surface gravity waves is strong. In particular, Surface Velocity Program (SVP) drifters have been designed to have the least influence of wave motions in their measurements thanks to a drogue centered around 15 m depth (Niiler & Paduan, 1995; Lumpkin et al., 2017). In the absence of that drogue, the drifter measures a not so clear combination of wind and surface cur-

67 rent speeds (Elipot et al., 2016). The surface drifts of Argo floats have also been used
 68 (Lebedev et al., 2007), and, for the lack of a better alternative, satellite remote sensing
 69 can be used, combining scatterometer winds, sea level anomalies from altimeters, and
 70 a combination of drifters and satellite gravimeters for the Mean Dynamic Topography
 (Rio et al., 2014).

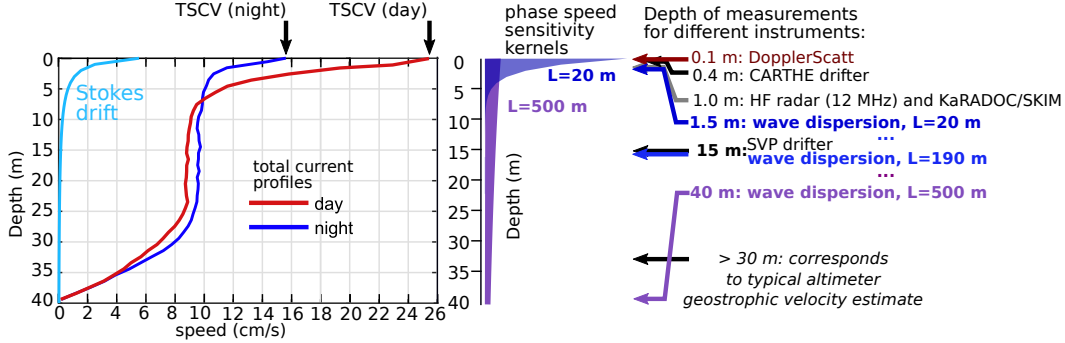


Figure 1. Left: typical day and night velocity profiles of the total current in the Atlantic at 26N , 36W (adapted from Sutherland et al. 2016). Center: sensitivity kernels for surface gravity wave phase speeds. Right: depth of measurement of different instruments. From top to bottom: DopplerScatt (Rodríguez et al., 2018), CARTHE drifters (Novelli et al., 2017), HF radars at 12 MHz (Stewart & Joy, 1974), near nadir Ka-band radars such as KaRADOC (Marié et al., 2020). The depth of measurement for wave dispersion is taken as the depth where a linear velocity profile matches the contribution of the current to the phase speed, namely $z = 0.08L$ where L is the considered wavelength (Stewart & Joy, 1974; Teague et al., 2001).

71

72 These estimates of the near-surface current can have significant differences, in
 73 part due to the sampling of different depths as illustrated in Fig. 1. Each measurement
 74 system provides a horizontal current velocity that is a convolution of the vertical
 75 profile of the velocity. For simplicity, it is convenient to define a "measurement depth"
 76 that can be taken as the depth at which a linearly varying current takes the given
 77 value. We note that DopplerScatt involves an empirical Geophysical Model Function
 78 and thus the physics of the measurement are not completely understood but the
 79 backscatter dominated by short gravity waves suggests a measurement depth under
 80 0.1 m, whereas near-nadir radar measurements, such as performed by the KaRADOC
 81 instrument (Marié et al., 2020) give a velocity that is weighted by the surface slope
 82 spectrum and corresponds to a measurement depth that does not vary much around
 83 1 m. It is thus desirable to measure the vertical shear of the current in order to be able
 84 to compare or combine these estimates from different observing systems. The shear is
 85 also an important indication of mixing or lack thereof, giving information on possible
 86 upper ocean stratification.

Shear estimates have used the wave dispersion modification due to the current vector, defined by the two components $U_x(z)$ and $U_y(z)$ of the horizontal current profile (Stewart & Joy, 1974). For completeness, a non-linear wave correction should also be included (Broche et al., 1983; Ardhuin et al., 2009), which is almost the same as replacing the Eulerian mean current by the Lagrangian mean current (Andrews & McIntyre, 1978). We thus expect, for $kD \gg 1$,

$$U(k, \varphi) \simeq U(k) \cos(\varphi - \varphi_U) = 2k \int_{-D}^0 U_x(z) \exp(2kz) \cos \varphi + U_y(z) \exp(2kz) \sin \varphi dz. \quad (1)$$

87

88 Obtaining current shear from a sequence of images has been done from many
 89 sensors including stereo-video imagery (Fedele et al., 2013), X-band radar (Campana et
 90 al., 2016) or polarimetric imagery (Laxague et al., 2018). In all cases it requires reliable
 91 estimates of $U(k, \varphi)$, for different wavelengths, including the shortest components,
 92 and this is performed by identifying propagating waves in the three-dimensional (3D)
 93 Fourier transform of the measured signals (Young et al., 1985; Peureux et al., 2018).
 94 A great opportunity is offered by satellite imagery with accurately co-registered views
 95 of the same ocean surface with short time lags. This is particularly the case of Sentinel
 96 2 imagery has been used to estimate surface current (Kudryavtsev et al., 2017b). The
 97 Sentinel 2 Multispectral Instrument (Drusch et al., 2012) has very strict co-registration
 98 requirements that make it possible to observe the signature of current velocities of the
 99 order of 1 m/s (Yurovskaya et al., 2019). Compared to methods that use a series of
 100 many images processed with a 3D Fourier transform, the analysis of only a few images
 101 is more difficult because of the very poor temporal resolution that does not give a full
 102 spectrum in the frequency domain. In particular the linear wave signal is not so easily
 103 separated from other contributions to the measurement.

104 The objective of the present paper is to discuss the influence of this limited time
 105 sampling on the accuracy of surface current estimates, in the presence of waves propa-
 106 gating in opposing directions, starting with the 2-image method used by Kudryavtsev
 107 et al. (2017b), as discussed in Section 2. In order to demonstrate the different pro-
 108 cessing steps and the influence of the image properties, we rely on the comparison of
 109 true data and simulated images generated using the simulator described in Appendix
 110 A. Due to the possible corruption of phase speeds by waves in opposing directions, we
 111 propose a new method using sequences of 3 images, as described in Section 3 with de-
 112 tails given in Appendix B. Discussions and conclusions follow in Sections 4 and 5. This
 113 paper does not address issues associated to systematic errors in the spatial registration
 114 on a global reference system with sub-pixel accuracy. These are partly discussed in
 115 Kääh et al. (2016) and Yurovskaya et al. (2019) and will be the topic of future work.

116 **2 Effect of waves in opposite directions with 2-image sun glint method**

117 **2.1 Short waves in opposing directions**

118 Pictures of the sun glint reveal wave patterns that are caused by the tilting of
 119 the sea surface by waves with wavelength larger than the pixel, adding their long
 120 wave slope to the local slope probability density function, and thus changing the pixel
 121 brightness. This effect has been described in many papers including Kudryavtsev et
 122 al. (2017a), and the geometry of the measurement is defined in Fig. 2. A key concept
 123 is that the surface can be decomposed in facets with a size of the order of 1 mm by 1
 124 mm, scale at which the sea surface is well approximated by a plane. There are thus
 125 a large number of such facets in a typical image pixel (10 m by 10 m for some of the
 126 bands of the MSI sensor on Sentinel 2) but the number of those that correspond to the
 127 specular direction can be relatively small, of the order of 100, while their brightness
 128 also varies, introducing random fluctuations in the image brightness.

As shown in Fig. 2.b for a spherical Earth, the satellite position S and observation
 point O correspond to a zenithal angle θ_v , related to the off-nadir angle γ by the law
 of sines,

$$\sin \gamma / R_E = \sin(\pi - \theta_v) / (R_E + H). \quad (2)$$

The time of acquisition of the different pixels is not available in the Level-1C
 Sentinel 2 product, but it can be retrieved from the provided view geometry. For
 example color band B01 is acquired at time t_1 when B02 is acquired at time t_2 , the
 time difference is given by the ratio of the angular distance $\alpha_{1,2}$ between the two nadir

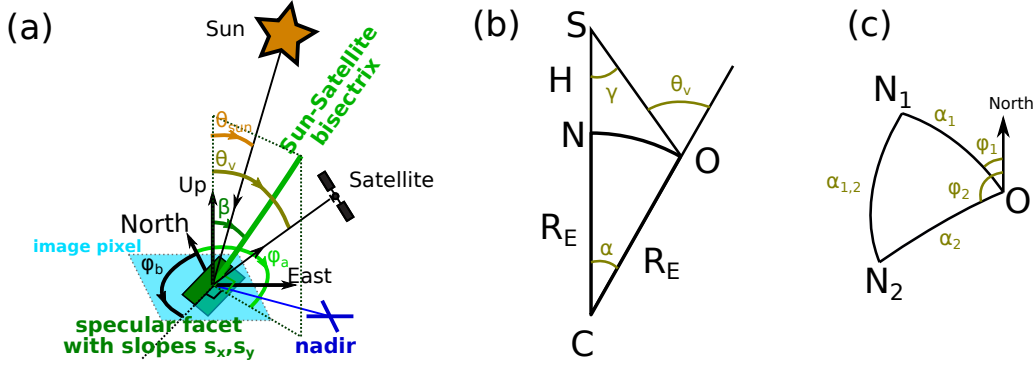


Figure 2. (a) Definition of viewing angles corresponding to a given sun and satellite sensor positions. The image brightness of a pixel is defined by the area of sub-pixel facets (in green) that gives a specular reflection and thus must have a given surface slope vector (s_x, s_y) . That area is proportional to the probability density function within that pixel for the slope (s_x, s_y) . This slope corresponds to the zenith angle β and azimuth φ_a . The perpendicular azimuths $\varphi_b = \varphi_a \pm \pi/2$ are "blind azimuths" in which the waves contribute a second order change to the pixel brightness and cannot be observed. (b) Position of satellite (S), observation point (O) and center of the Earth (C) in a vertical plane. (c) Triangle on the sphere joining the observation point O and the nadir positions N_1 and N_2 at observation times 1 and 2.

points N_1 and N_2 , as depicted in Fig. 2.c, and the angular speed along the orbit Ω (in rad/s). The angular distance $\alpha_{1,2}$ is obtained from the law of cosines on the sphere,

$$\cos \alpha_{1,2} = \cos \alpha_1 \cos \alpha_2 + \sin \alpha_1 \sin \alpha_2 \cos(\varphi_2 - \varphi_1). \quad (3)$$

129 This typically gives distances and time lags within 1% of the expression given by eq.
 130 (1) in Yurovskaya et al. (2019).

131 In order to illustrate the limitations of the 2-image method, we start from the
 132 same image example that was used in Kudryavtsev et al. (2017a), acquired off the
 133 California coast in the region of San Diego. The image processing method is illustrated
 134 in Fig. 3. In order to understand the processing results, we also have generated
 135 simulated images and applied the exact same processing to the them.

136 The image simulator is described in more detail in Appendix A, and corresponds
 137 to the forward model of Kudryavtsev et al. (2017a), combined with a noise model. For
 138 our first example, the model input parameters are the Sentinel 2 viewing geometry,
 139 an estimate of the surface wind vector given by satellite scatterometer data, and a
 140 directional wave spectrum that is estimated from an *in situ* buoy. The buoy is station
 141 number 220 of the Coastal Data Information Program (CDIP) located at 32.752N
 142 117.501W, also identified by the World Meteorological Organization with the number
 143 46258.

144 In order to obtain a more robust estimation of the current speed, we used a phase
 145 estimated from the coherent sum of the complex amplitudes obtained from individual
 146 image tiles that are 500 m wide. We first sum the $16^2=256$ tiles, and then add 15^2 tiles
 147 that are shifted by 250 m in each direction in order to use the signal that is otherwise
 148 much reduced by the 2-dimensional Hann window, but is these shifted windows are
 149 not independent samples. This gives 256 independent estimates of the phase and
 150 associated current for each spectral component. The main information that we shall

151 use is the phase difference $\psi_{i,j}(k, \varphi)$ between the bands number i and j , for the spectral
 152 component with wavenumber k propagating in azimuth φ .

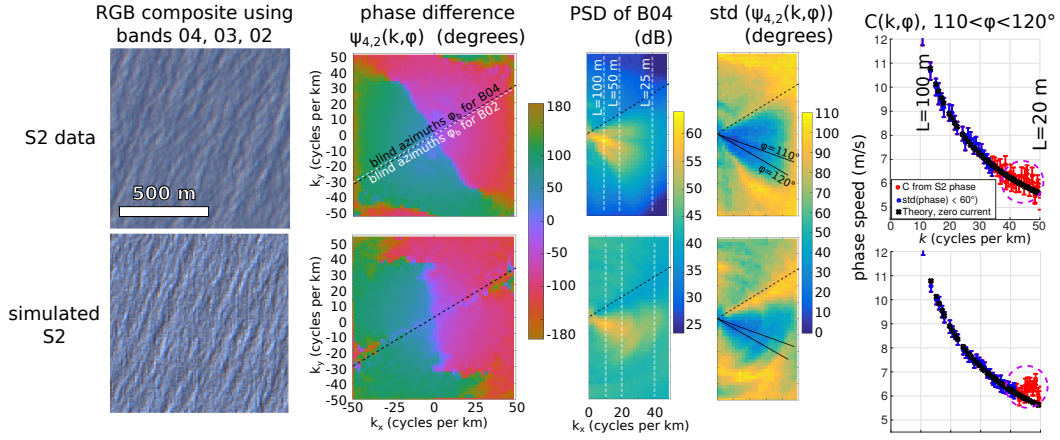


Figure 3. Example of processing from Level-1C images to phase speeds, using 500 x 500 m tiles over a 8 by 8 km area. Top: data from Copernicus Sentinel 2 on 29 April 2016 off California (See Figs. 3-9 in Kudryavtsev et al. 2017), with $\beta = 9^\circ$, $U_{10} = 6$ m/s. Bottom: simulated Sentinel 2 data based on *in situ* wave spectrum determined from directional moments using the Maximum Entropy Method, and with random phases. The multiplicative noise amplitude is set to $N_t = 0.15$. The present paper was motivated by the phase speed anomalies, highlighted with the dashed magenta circle near the Nyquist wavelength $L = 20$ m.

152

By definition the phase changes sign for opposite directions $\psi_{i,j}(k, \varphi) = -\psi_{i,j}(k, \varphi + \pi)$, and this phase difference can be interpreted as the result of the propagation of a single wave component at speed

$$C(k, \varphi) = \psi_{i,j}(k, \varphi) / [k(t_i - t_j)], \quad (4)$$

153 where t_i is the acquisition time for band i . Most of our analysis of Sentinel 2 data is
 154 based on the bands B04 and B02 giving a phase $\psi_{4,2}(k, \varphi)$.

155 The shortest waves that propagate along the x or the y axis in the image have a
 156 20 m wavelength. Their phase speed, for zero current, is expected to be 5.6 m/s and
 157 thus the wave patterns should be displaced by 5.6 m between the red and the blue
 158 channels that are separated by 1.0 s, and only 2.8 m between the red and green. This
 159 distance is shorter than the 10 m pixel size, but comparable to the requirement for
 160 co-registration of the MSI sensor set to 3 m for 3 standard deviations (Drusch et al.,
 161 2012) In other words, Sentinel 2 can detect wave motions, but is the instrument and
 162 processing accurate enough to detect the generally smaller variations in phase speed
 163 associated to currents? In fact, Fig. 3 shows that the phase speeds down to 25 m
 164 wavelength are consistent with linear wave theory but large fluctuations of the order
 165 of 1 m/s are found between 25 m and 20 m wavelengths, and these vary strongly with
 166 the choice of azimuth φ . Such fluctuations are not included in the surface current
 167 estimates made by Yurovskaya et al. (2019), because these authors exclude spectral
 168 components with a coherence under 0.8. This coherence, denoted "coh" in the following
 169 equations and figures, is also called magnitude-squared coherence. We note that this
 170 threshold is equivalent to a standard deviation of the co-spectrum phase ψ of 40° ,
 171 because for small values of the phase ψ in radians, $\text{std}(\psi) \simeq 2\sqrt{1 - \text{coh}}$.

172 If the vertical shear in the top few meters is to be measured, we have to use
 173 these shorter wave components. Presumably we could use spectral components with
 174 a lower coherence, hence a larger uncertainty, and use the averaging over a larger
 175 number of spectral components to mitigate this larger uncertainty. For the shorter
 176 components, with $k \simeq 40$ cpkm, the coherence is under 0.35 for all directions, and
 177 highest for $110 < \varphi < 120^\circ$, with a corresponding fluctuation of the phase $\text{std}(\psi) \simeq$
 178 70° . Interestingly, the same low coherence and high level of phase fluctuations are
 179 also present in the simulated data, even when the noise level is reduced to zero. We
 180 found that this pattern was not associated to the amplitude nor to the additive or
 181 multiplicative nature of the noise in eq. (A1), nor even the non-linear modulation
 182 transfer function. The low coherence persists as long as some energy remains for
 waves in opposing directions. These fluctuations in the phase speed for the shortest

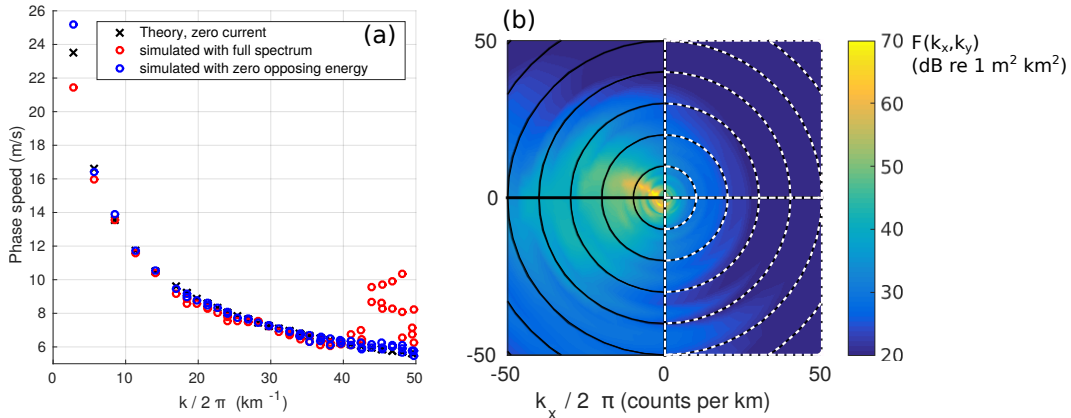


Figure 4. (a) Phase speeds for the simulated image in which either the full spectrum $F(k_x, k_y)$ is taken or the right half of the spectrum $F(k_x \geq 0, k_y)$ is set to zero to have zero opposing wave energy, for directions $130^\circ \leq \varphi \leq 140^\circ$. (b) Wave spectrum estimated from buoy data and used in the simulation, energy is represented in the direction from which waves are coming, i.e. corresponding to negative frequencies

183 wave components disappear in the simulation when the input spectrum is "chopped"
 184 to remove waves propagating from the east (with $k_x < 0$, see Fig. 4). Clearly, the
 185 spurious large values of phase speeds for wavelengths $20 \text{ m} < L < 25 \text{ m}$ are associated
 186 to a significant level of energy in opposing directions.
 187

188 Any spectral component (k, φ) contains information that propagates in both
 189 directions φ and $\varphi + \pi$. By interpreting the phase difference $\psi_{1,2}$ as the phase of a
 190 single travelling wave, in direction φ if the phase speed is positive, we are assuming that
 191 we can neglect the waves in the opposite direction. In fact, the data is in general the
 192 sum of two wave trains travelling in these opposite directions, each giving a different
 193 contribution to the phase difference $\psi_{1,2}$, one of these two can be neglected if its energy
 194 is much weaker (typically with a difference of 20 dB or so), which is not the case in
 195 our example for $L < 25 \text{ m}$. The magnitude of wave energy in opposing directions for
 196 wavelengths under 20 m has been particularly studied for the retrieval of surface wind
 197 direction using HF radar (e.g. Kirincich, 2016), but few studies have been performed
 198 for longer wavelengths (Tyler et al., 1974).

In order to quantify the magnitude of waves in opposing directions, we define an "opposition spectrum",

$$H(k, \varphi) = \frac{4E(k, \varphi)E(k, \varphi + \pi)}{[E(k, \varphi) + E(k, \varphi + \pi)]^2}. \quad (5)$$

As defined, H ranges from 0 for waves propagating only in direction φ , to 1 for equal amplitudes in opposing directions φ and $\varphi + \pi$. This is the directionally-distributed counterpart of the "overlap integral" $I(k)$ defined by Farrell and Munk (2008). $I(k)$ was first used by Hasselmann (1963) and Brekhovskikh et al. (1973) for the theory of generation of secondary microseisms and microbaroms (see Ardhuin et al., 2015; De Carlo et al., 2020, for recent reviews). If $H(k, \varphi)$ is independent of φ then $I(k) = H(k, \varphi)$.

Starting from the same wave spectrum as in Fig. 4, we have simulated images with different noise levels N_t and replaced the spectral level in the left-propagating components ($0^\circ < \varphi < 180^\circ$) with values given by a constant r times the values at $\varphi + \pi$, giving a constant $H = 4r/(r + 1)^2$. The result of these academic tests is shown in Fig. 5. Looking at the mean error for the current U and the standard

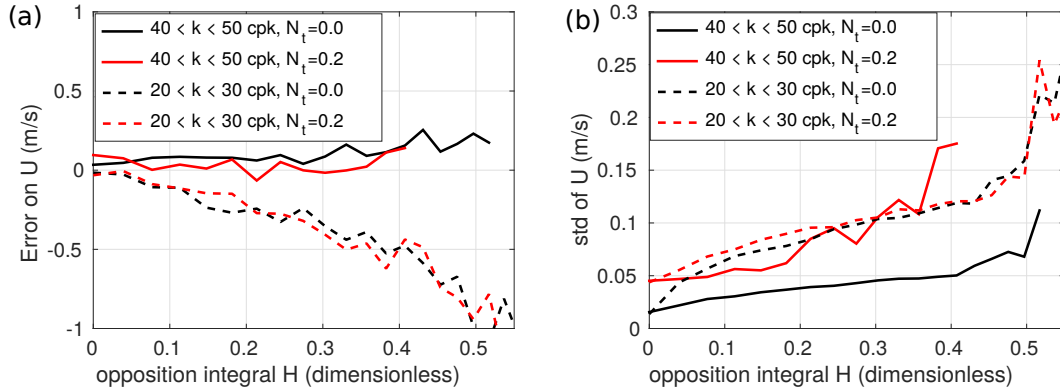


Figure 5. Errors in current retrieval for directions $110^\circ < \varphi < 120^\circ$ as a function of the opposition spectrum H using the same simulated spectrum as in Figure 4. (a) Mean current value (and thus error since the input current is zero) (b) standard deviation of the current.

deviation of the value of U , it is clear that a larger opposition spectrum gives a larger error. Part of the larger error comes from a larger number of spectral bins for which the standard deviation of the cross-spectral phase is larger than 60° and are thus not included in the average. That effect also explains why no value is shown for $N_t = 0.2$ and $H > 0.41$: all spectral bins in that case had a $\text{std}(\psi) > 60^\circ$. Even for $N_t = 0$, the presence of opposing waves leads to very large biases on U that cannot be detected by inspecting only $\text{std}(\psi)$. In other words, it may not be feasible to flag errors caused by the the waves in opposing directions when using the co-spectrum phase to estimate the surface current. For the case shown in Fig. 5.a, the error can be up to 0.25 m/s for $H = 0.2$, which would be the value given right off the coast by a 5% coastal reflection, which is a typical value for steep beaches or rocky shores (Ardhuin & Roland, 2012). These results are very robust and do not change qualitatively when changing the shape of the wave spectrum. We suspect that the general larger errors for smaller wavenumbers are associated to the smaller phase shift of the longer waves, corresponding to a lower signal to noise ratio.

226

2.2 Coastal reflections and longer wave components

227

228

229

230

231

232

We may look for further evidence for the effect of waves in opposing directions by looking at recent images acquired off the Oahu north shore, Hawaii on 23 May 2020, as shown in Fig. 6. Error bars on the phase speeds on Fig. 7b,d,f,h correspond to ± 1 standard deviation of the phase speed, divided by the square root of the number of independent spectral estimates, giving an uncertainty on the average assuming a Gaussian distribution.

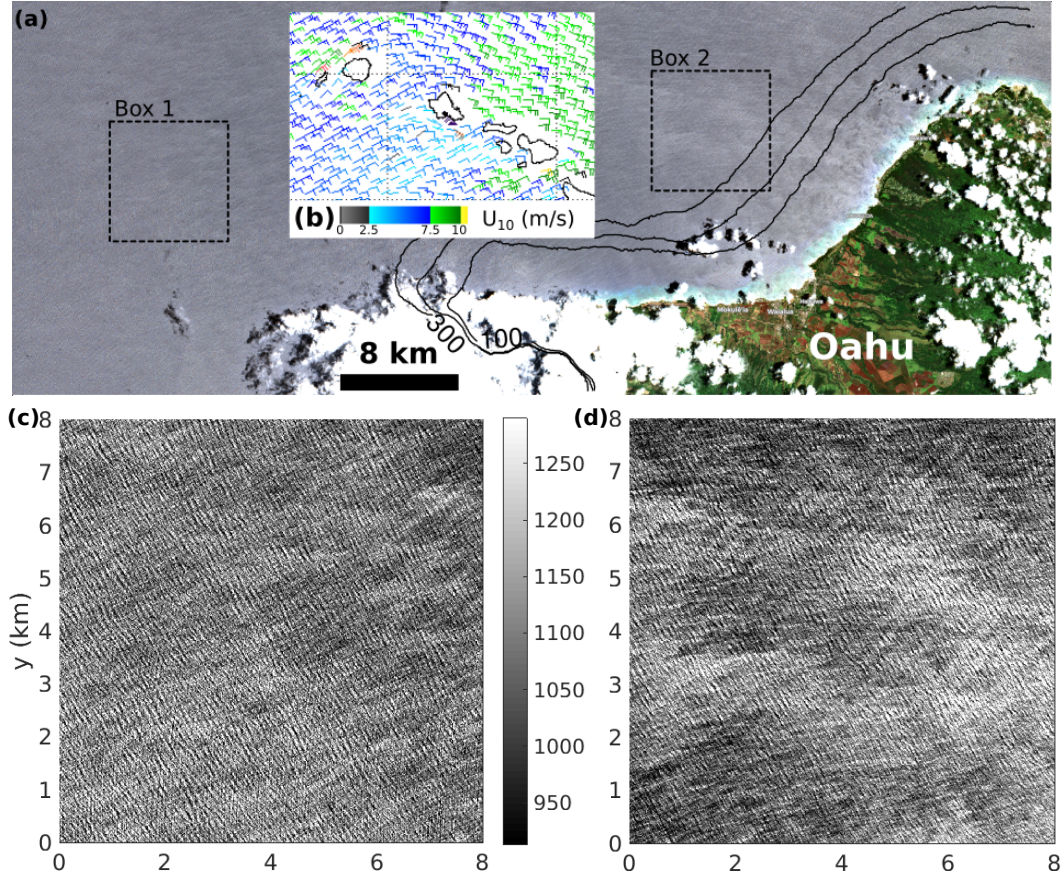


Figure 6. Sentinel 2 image off the North Shore of Oahu. (a) True color image and location of analysis boxes 1 and 2. (b) Wind speed and direction from ASCAT. (c) and (d) are the channel B04 values for Box 1 and Box 2 respectively.

233

234

235

236

237

238

Previous work by Ardhuin and Roland (2012) has found evidence of significant coastal reflection, with an energy reflection coefficient of the order of 10%, that would give $H \simeq 0.3$ right at the shoreline, a value that decreases away from the shore as the reflected part of the wave spectrum is broadened by the variability of the shoreline direction and refraction. Numerical simulations of the sea state typically give $H < 0.1$ in Box 2. As a result, the effect of shoreline reflection is rather weak.

239

240

241

242

243

Looking at the the dispersion of 250-300 m wavelength from the North-West, there is a narrow spectral peak (Fig.7.a) with phase speeds in the range 10 m/s to 20 m/s (Fig.7.b). However, Box 2 has very similar noise levels and phase speeds. In both cases, the estimated phase speed is very far from the linear phase speed, and the O(5 m/s) difference cannot be reasonably attributed to the current. Our interpretation

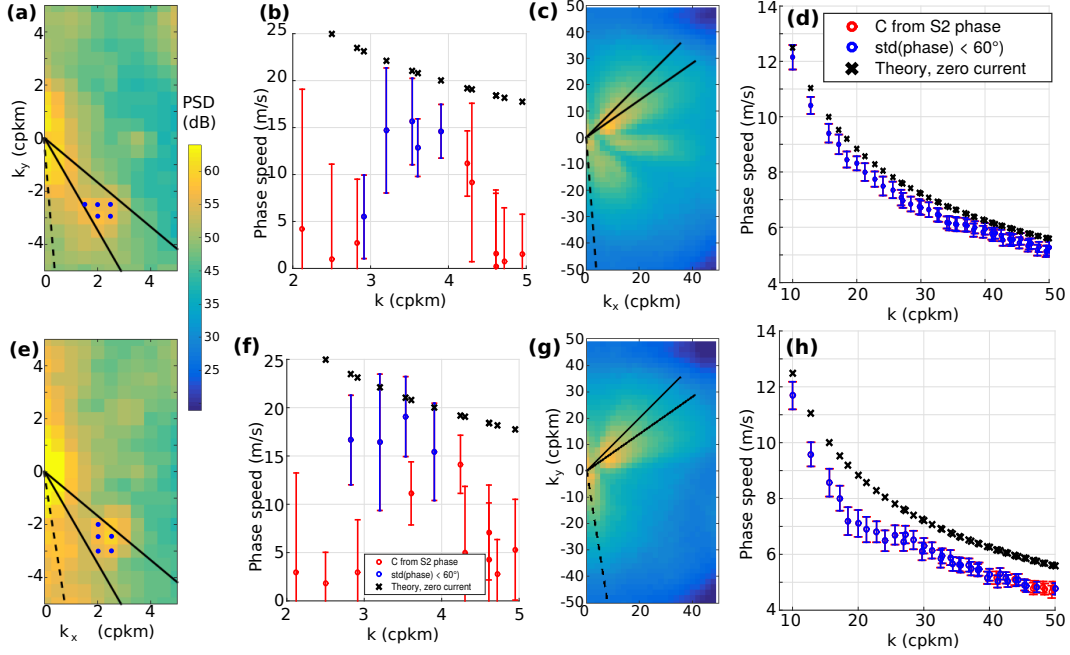


Figure 7. Analysis of 2 pieces of the S2 image shown in Fig. 6. For Box 1, (a) shows the PSD of the image intensity obtained with 2 km by 2 km tiles to give a better spectral resolution for wavelengths around 300 m, with dots marking the “low noise spectral components” that give a standard deviation of the co-spectrum phase under 60° and (b) the phase speed of long wave components with directions between 130° and 150° , with blue bars corresponding to those low noise spectral components. (c) and (d) were obtained with 500 m by 500 m tiles focusing on shorter waves with directions between 45° and 55° . (e) to (h) show the same quantities for Box 2. The dashed lines in panels (a),(c),(e),(g) indicate the blind azimuth (see Fig. 2 for its definition) and the blue dots in (a) and (e) indicate the spectral components for which the $\text{std}(\text{phase})$ is less than 60° , with velocity estimates shown with blue symbols in (b) and (f).

244 is that the phase difference between the B04 and B02 images is biased low because
 245 some of the estimates are dominated by noise, even though our coherent sum of the
 246 co-spectra was weighted by the spectral energy. In this case the strongest spectral
 247 component in (Fig.7.e) with $k_x = 2.5$ cpkm and $k_y = -2.5$ cpkm is the one with the
 248 largest velocity magnitude (17 m/s) in (Fig.7.f), but the random distribution of phases
 249 gives an uncertainty of ± 3 m/s, and the coherence is 0.94.

250 Looking at the full spectrum, we find that all the velocities are also probably
 251 biased by an error in the relative position (co-registration error) of the two bands
 252 B04 and B02, and/or an error in the time lag. Whereas the given geometry of the
 253 measurements gives a time lag of 1.00 s, it would take a roughly 1.0 m/s current in
 254 azimuths $20^\circ < \varphi < 80^\circ$ to explain the measured phase speeds for k in the range 30
 255 to 40 cpkm, and the estimated current should vary like $\cos(\varphi - \varphi_U)$. Instead, the
 256 observed wave dispersion is more consistent with a time lag of 0.87 s and a much
 257 weaker current. That time lag difference of 0.13 s, with a phase speed of 7 m/s is also
 258 equivalent to a bias of 0.9 m in the location of the pixels, that could be caused by a
 259 bias of 1 microradians in the knowledge of the relative pointing of the different bands
 260 for the same detector. We also note that the 1 m/s order of magnitude of the possible
 261 error on the current velocity is consistent with the spurious stripes appearing in maps

of surface current estimated by Yurovskaya et al. (2019) and O(1 m) co-registration errors found by Kääh et al. (2016).

More interestingly for the purpose of the present paper, the variation of phase speed as a function of wavenumber has a O(50 cm/s) anomaly in box 2 for k around 20 cpkm. Could that be the signature of a current maximum at a depth around 10 m? In the absence of verifying measurements we cannot explore this with any certainty.

3 Least squares method applied to a sequence of 3 images

Going back to the problem of estimating phase speeds for the shorter wave components that often have relatively large values of H , we propose to try to separate the waves in opposing directions, and for this, use more than two images. This problem is very similar to the problem of separating waves in opposing directions in wave laboratory experiment, which is necessary for implementing absorbing boundary conditions at paddle wave makers. The founding paper in this line of work was the method of Mansard and Funke (1980) for computing wave reflection using a series of 3 wave gauges with a least square method. It was later improved on by Zelt and Skjelbreia (1993). We are not aware of an adaptation to image processing and generalization of the method to estimate currents at the same time as the amplitudes of the two opposing wave trains. As detailed in the Appendix B, this generalization is straightforward.

We first test the method for simulated monochromatic waves of 50 m wavelength propagating in one dimension and resolved at $dx=10$ m resolution with time lags of 0.5 and 1.0 s similar to the red, green and blue bands (B04, B03, B02) of Sentinel-2. We found that adding one extra measurement at a 0.8 s lag, similar to band B08 on Sentinel-2, had a limited impact on the results. The method is illustrated in Fig. 8 with spatial series, with or without noise. With a small value of the opposition spectrum, here $A = 1$, $B = 0.1$ and thus $H \simeq 0.04$, (except for $B = 0.2$ in Fig. 8.a), the wave field looks like a single propagating wave with a modulated amplitude, changing from 1.1 to 0.9 over half a wave period, here 2.8 s, due to the partial standing wave. When multiplicative noise is added, the distribution of current estimates from phase differences is Gaussian for waves propagating in only one direction (Fig. 8.c). In the case of the least square method, the distribution has heavier tails than a Gaussian distribution and thus requires a very broad range of velocities to be properly characterized. In our example, the uncertainty is 20 times larger when using the least square method (see Fig. 8.b compared to 8.c). In contrast to A and B , we do not have an analytical expression for U and it is difficult to predict its distribution. In practice, we find that the median of the distribution of U is apparently not biased (Fig. 8.b,d,f), and the mean of M estimates of this median apparently converges following the central limit theorem with a standard deviation reduced by $1/\sqrt{M}$. One may thus hope to retrieve the current with this method, even for noisy data.

We note that the uncertainty on the current U , as measured by the standard deviation of the distribution of U , is not affected by the presence of waves in both directions when using the least square method: changing the value of B from 0 (Fig. 8.b) or 0.05 (Fig. 8.d) to 0.1 has no influence on the distribution (not shown). With the least square method the current uncertainty generally decreases when reducing the noise (Fig. 8.d) or increasing the signal, for example when increasing the time differences between the measurements (Fig. 8.f). In contrast, when waves in opposing directions are present, the error reduction in the phase method is very limited when the noise is reduced (Fig. 8.e). Both methods are improved when the time lag is increased by a factor 10, as shown in Fig. 8.f,g.

We now apply the least-square method to actual Sentinel 2 imagery, with 3 bands (B02, B03, B04). We first note that the image amplitude and standard deviations are

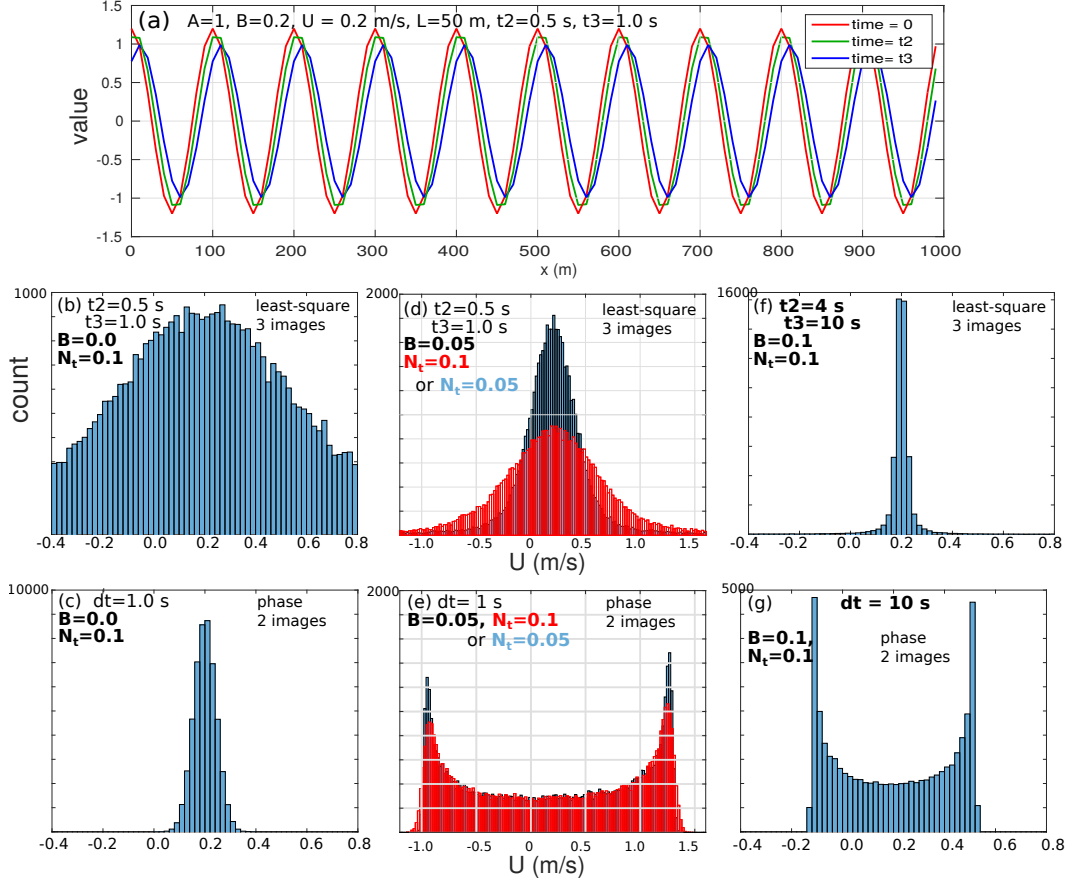


Figure 8. (a) Example of 3 spatial series at 3 different times in the presence of rightward propagating and leftward propagating waves of wavelength $L = 50$ m, amplitudes $A = 1$ and $B = 0.2$ and a $U = 0.2$ m/s current. The time lags of 0.5 and 1 s are typical of Sentinel 2 data for the 10 m resolution R, G, and B channels. (b–g) Monte-Carlo simulations of the estimation of the current velocity U from 50000 monochromatic spatial series with white multiplicative noise of amplitude N_t , using least squares in (b,d,f), and using the phase difference between 2 images in (c,e,g). For reference the distribution of estimated currents is also shown in (b,c) when the amplitude of leftward propagating waves is zero.

312 different for the different bands, so that the shift from one band to another is not just
 313 a propagation but also includes a change in mean value and amplitude. In order to
 314 mitigate that effect we have shifted and rescaled the pixel values so that each image
 315 has a zero mean and unit standard deviation before computing Fourier transforms.

316 We first take up our example off California, with results shown in Fig. 9. Noisy
 317 parts of the spectrum generally correspond to a low coherence in image pair (Fig. 9.a)
 318 and a high uncertainty for the co-spectrum phase (already shown in Fig. 3) and hence
 319 current velocity. When using a least square fit, an obvious candidate for quantifying
 320 the noise is the residuals that we have normalized by the sum of the spectral densities
 321 of the images.

For each spectral component (k, φ) and each m -index sub-image of 100 by 100 pixels we fit the amplitudes $Z_{A,m}(k, \varphi)$ of a wave train travelling in direction φ and $Z_{B,m}(k, \varphi)$ travelling in direction $\varphi + \pi$ and the current velocity $U_m(k, \varphi)$ that min-

minimizes the sum of square residuals that is the difference between the image spectral density $B_{n,m}(k, \varphi)$ and our model of two counter-propagating components (See appendix B). We only keep values of U that fall in the range from -5 to 5 m/s, for which there is a number $M(k, \varphi)$ of estimates. For each spectral tile we have a normalized residual,

$$\varepsilon_m(k, \varphi) = \sqrt{\sum_n |\varepsilon_n(k, \varphi)|^2 / \sum_n |B_n(k, \varphi)|^2}. \quad (6)$$

From these "successful fits", their number is $M(k, \varphi)$, we take the current to be the median of the $U_m(k, \varphi)$ values and we define a root mean square residual,

$$\varepsilon_r(k, \varphi) = \sqrt{\sum_m \varepsilon_m^2 / M(k, \varphi)}. \quad (7)$$

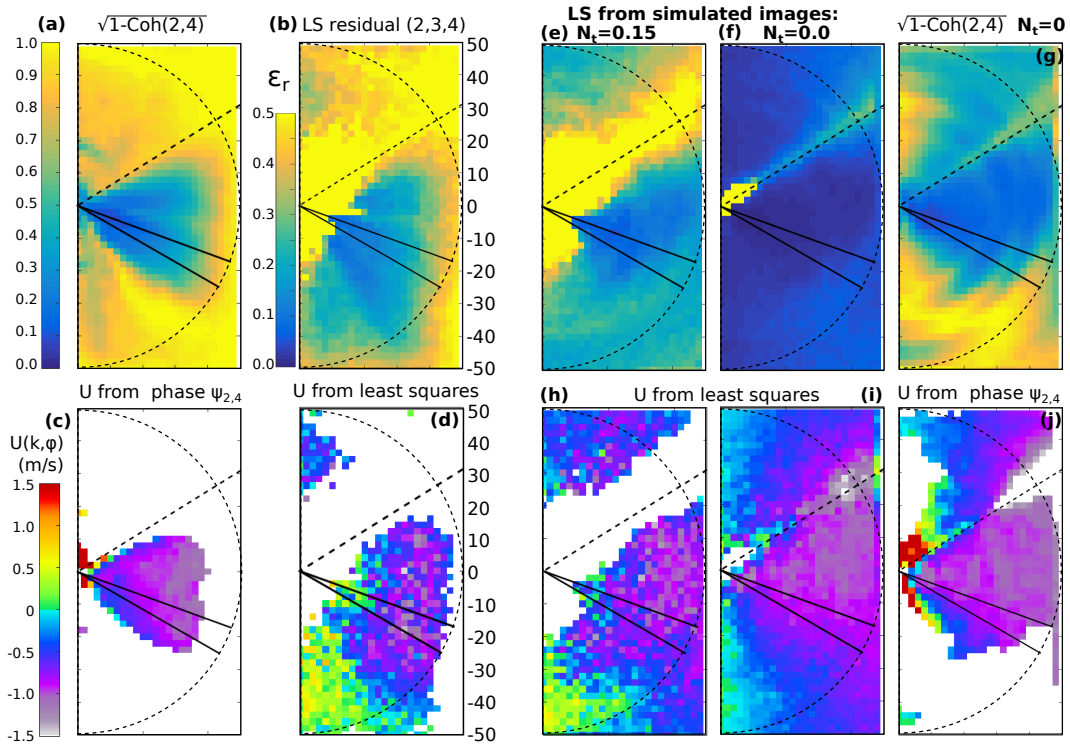


Figure 9. All the panels show quantities in spectral space ($0 < k_x < 50$ cpkm, $-50 < k_y < 50$ cpkm). Top panels (a,b,e,f,g): Error metric (coherence for phase method, standard deviation of normalized residual for least-squares method) Middle panel (c,d,h,i,j): Estimate of velocity in φ direction. The dashed circle corresponds to $k = 50$ cycles per km. The simulated images includes a non-zero current vector $\mathbf{U} = (-1, 0)$ m/s, so that the current component in direction φ should be $-\sin(\varphi)$, very close to what is retrieved in panel (i).

322 Inspecting (Fig. 9.b) we propose that a first not-too-conservative but reasonable
 323 threshold for acceptable results is $\varepsilon_r < 0.4$, giving the current values shown in Fig.
 324 9.d. This choice was motivated by the desire to include the spectral components for
 325 which we found that waves in opposite direction were a significant source of error for
 326 the phase method, but this also keeps spectral components with very low signals (with
 327 azimuth directions between 0° and 30° , and between 135° and 180°).

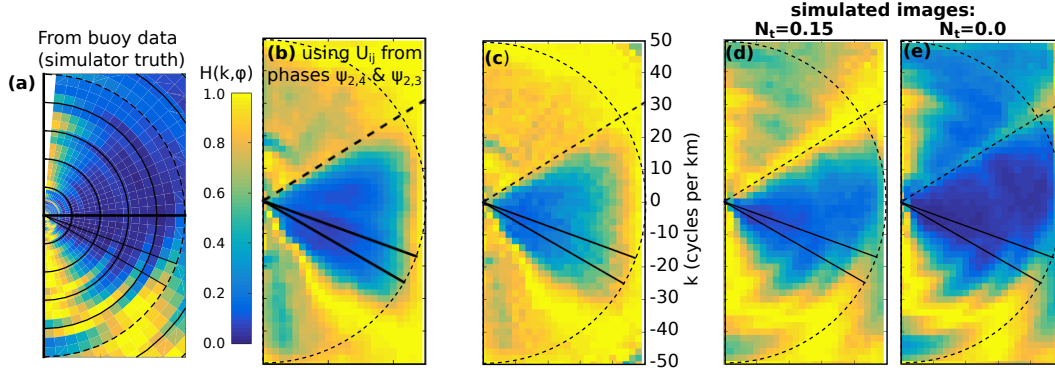


Figure 10. Estimates of the opposition spectrum $H(k, \varphi)$, for the spectral range ($0 < k_x < 50$ cpkm, $-50 < k_y < 50$ cpkm). Panel (a) shows the H spectrum based on the MEM-estimated spectrum from the in situ buoy, (b) and (c) show two estimates from the Sentinel 2 image using either the current estimated from phase differences or the current also given by the least squares method. (d) and (e) are the results for simulated images with different levels of noise.

In addition to the current, we also estimate the opposition spectrum as

$$H(k, \varphi) = \frac{4|Z_A|^2(k, \varphi)|Z_B|^2(k, \varphi)}{(|Z_A|^2(k, \varphi) + |Z_B|^2(k, \varphi))^2}. \quad (8)$$

328 Although we have no direct measurement of the true directional spectrum $E(k, \varphi)$ and
 329 thus of $H(k, \varphi)$ using eq. (5), we may compare estimates H_i to the values shown in Fig.
 330 10.a and given by the wave spectrum estimate $E(k, \varphi)$ using the Maximum Entropy
 331 Method, which is used in the image simulations. It is not clear at all if the MEM
 332 derived spectra give values of $H(k, \varphi)$ that should have the same order of magnitude
 333 as those given true directional spectrum. This question could be investigated with
 334 stereo-video data (e.g., Guimarães et al., 2020).

335 When using the least square estimate of Z_A and Z_B that correspond to the least
 336 square estimate of U for each image tile, the values recovered from the S2 image are
 337 typically much higher than those estimated from the buoy as shown in Fig. 10.a) : in
 338 the range 0.2 to 0.4 for the part of the spectrum that has a coherence squared higher
 339 than 0.64 which is already lower than the 0.8 threshold in Yurovskaya et al. (2019).
 340 This value of H is probably at least 10 times too high around the spectral peak. These
 341 would typically give a background level of microseism sources that is too large by a
 342 factor 10 or more. What happens is that the fitting procedure puts some of the noise
 343 in the amplitude of the opposing waves. As a result, a lower threshold than $\varepsilon_r < 0.4$
 344 is necessary to give accurate estimates of the opposition spectrum H . But we can also
 345 force the current to the value estimated from the phase method and only fit Z_A and
 346 Z_B , in that case the values of H are more realistic, as shown in Fig. 10.b.

347 For that estimate we have also modified the equations in Appendix B to allow
 348 for a different current at times t_2 and t_3 in order to absorb the biases in the image
 349 position $(\delta X, \delta Y)_{i,j} = (U_{ij}, V_{ij}) \times (t_j - t_i)$. Indeed the phase difference $\psi_{2,3}$ gives
 350 a velocity vector close to $(-1.8, 0)$ while $\psi_{2,4}$ gives $(-1, 0)$ corresponding to a 1 m
 351 eastward erroneous shift of the B02 image relative to B03 and B04. This inconsistency
 352 in the data is not included in the fitted model proposed in Appendix B and thus
 353 contributes to higher errors in the estimate of U . One possibility may be to recompute
 354 the least squares with different velocities over the different time lags, or to use the
 355 phase difference method on all image pairs to estimate deviations from a constant
 356 speed and shift the image before applying the least square method.

357 For our test image, it is thus dubious that the least-square method, as imple-
 358 mented here, has provided any additional reliable information for short waves com-
 359 pared to the phase method. Using a more conservative threshold $\varepsilon_r < 0.2$ it is possibly
 360 able to slightly extend the part of the spectral plane from which a velocity can be de-
 361 rived to directions that are further away from the mean wave direction.

362 Looking beyond the particular case of the bands B02, B03 and B04 of the Sen-
 363 tinel 2 sensor, it is interesting to know how well this method may work. We have thus
 364 simulated the image and its processing, and reduced the noise level from $N_t = 0.15$
 365 (which looks similar to the true Sentinel 2 image) to no noise at all with $N_t = 0$.
 366 Without any noise, the least square fit is very good with $\varepsilon_r < 0.1$ for the full spec-
 367 tral domain, except around the blind azimuth. As a result the input current vector
 368 $\mathbf{U} = (-1, 0)$ m/s is very well recovered. This would not be the case for the shortest
 369 components using the phase method except in the mean direction, giving only one
 370 component of the current vector.

371 The precision on the retrieval of the surface current is further illustrated in Figure
 372 11, focusing on a narrow range of azimuths, between 110 and 120° . The error bars
 373 give an estimate of the precision of the mean within each spectral bin that are all
 374 completely independent. For the phase-difference method, the smooth variation of
 375 the estimates across the spectra (within the error bar) confirm that the $O(15 \text{ cm/s})$
 376 precision for each spectra estimate is realistic. This does not say anything about the
 377 accuracy of the estimate that is dominated by an $O(1 \text{ m/s})$ error due to relative pixel
 378 co-registration errors of the different bands.

379 For the least-square methods, the error bars are more difficult to define given
 380 the heavy tails of the U distribution and the sample size (256 independent spectra
 381 giving 256 estimates of U). It might be possible to use the distribution of residuals ε_m
 382 obtained for the M spectra as given by eq. (6), because they are correlated with errors
 383 on U , but we have not found a satisfactory parameterization that would work for both
 384 the academic 1D case of Figure 8 and the true images. If needed, the only robust
 385 uncertainty we can propose is to compute the standard deviation across neighboring
 386 spectral components, for example in a 10 cpkm band of wavenumbers. Both the phase
 387 and least square methods agree in the range 25 cpkm to 35 cpkm but there are large
 388 biases of the least-square method for both short and long components as shown in
 389 Fig. 11.a. Although some of these errors could be caused by instrument errors (such
 390 as errors in the retrieved observation angles that could change the estimate time lags
 391 and distort the dispersion relation), it is striking that the simulated data shown in
 392 Fig. 11.b gives similar errors, but slightly weaker, which leads us to think that the
 393 biases in the least square method may be dominated by artefacts of the processing
 394 method. We have not yet identified the source of these errors. We also note that the
 395 phase method, in contrast, has no trend in the simulated data for which the standard
 396 deviation of the phase is under 60° .

397 We generally expect that errors can be reduced by increasing the time separation
 398 of the images so that the mean phase difference is much larger, making random phase
 399 differences comparatively smaller. Fig. 11.c,d shows that realistically noisy images
 400 with a doubled time lag are preferable to a noise-free image with the same time lag.
 401 This is easy to understand in the case of the phase difference method: the larger
 402 phase difference makes the random-phase noise a relatively smaller term in the phase
 403 difference. The uncertainty on U is inversely proportional to the time difference.

404 A first verification of this advantage of larger time lags is provided by using the
 405 B12 and B11 band, that are acquired 1.1 s and 0.5 s before B04, which is here 1 s
 406 before B02 (this ordering correspond to the even detectors on S2, it is reversed for the
 407 odd detectors). Hence combing B12 with B11 and B02, giving a maximum time lag of
 408 2.1 s . Because the spatial resolution of B12 is only 20 m , we have averaged B02 over

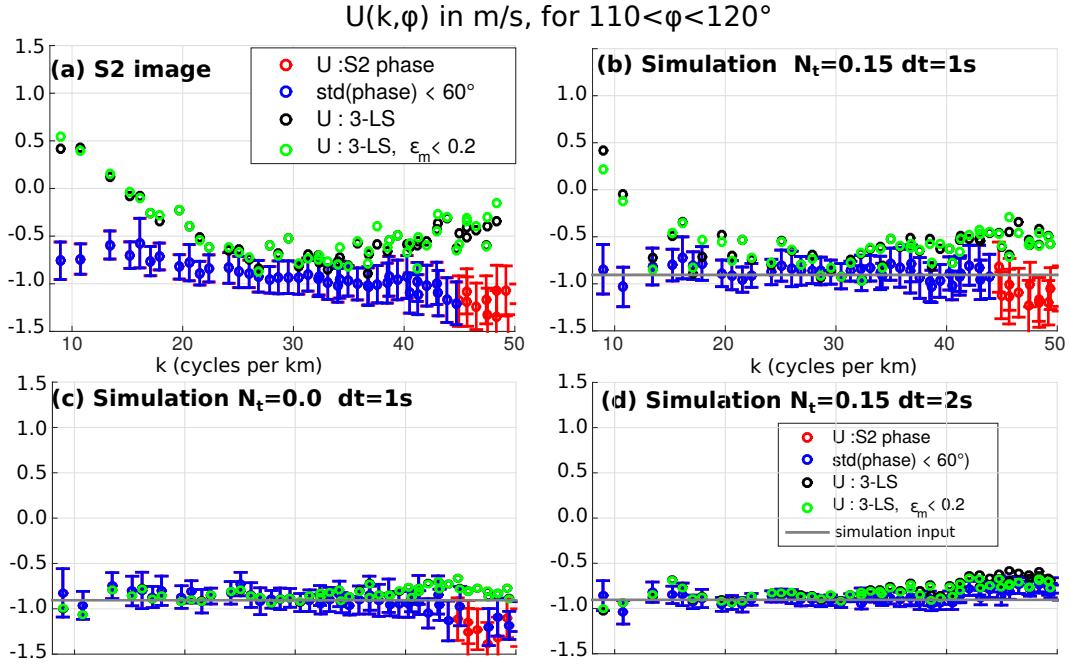


Figure 11. Comparison of different current estimates for waves in azimuths 110° to 120° for (a) Sentinel 2 data using bands B04, B03 and B02, and simulated data with the (b) same time lag and similar noise level, or (c) no noise, or (d) a doubled time lag. For the phase difference method (red and blue symbols) the error bars shows the mean value obtained for each spectral component plus or minus one standard deviation divided by the square root of the number of estimates. We have also tested (in green) using a sub-sample of the least-squares, keeping only those with small values of the residual ε_m .

409 2 by 2 pixel boxes to provide images at the same resolution, including a 1 m westward
 410 shift of B02 to corrected for the error noted above. These results are illustrated in Fig.
 411 12.

412 We first note that the shape of the spectrum, here resolved at higher spectral
 413 resolution, shows a 3-lobe structure with minima of the image PSD and coherence
 414 for the azimuths 100° and 125° , these are probably due to artefacts of the Level 1-C
 415 processing. For the waves in the direction of highest coherence, $108^\circ < \varphi < 118^\circ$, the
 416 uncertainty on U obtained in the range of wavenumbers 10 to 20 cpkm is as low as
 417 0.1 m/s in spite of the average of only 64 independent tiles (compared to 256 for Fig.
 418 11.a). Combining all the 25 spectral components available from 10 to 20 cpkm gives
 419 an uncertainty of 3.4 cm/s, which we estimated from the mean of the uncertainties
 420 divided by the square root of the number of spectral components. Performing the
 421 same analysis on 20 m box averages of B03 and B02 gives a 5.8 cm/s uncertainty. It is
 422 therefore beneficial to use the largest time lags for estimating the current speed from
 423 wavelength between 50 and 100 m. We note that the least square method gives rather
 424 puzzling results that we do not understand, with a variation of the estimated current
 425 as a function of wavenumber that is large and not random.

426 In the case of the waves shorter than 40 m wavelength, that are only resolved
 427 in the 10 m images such as given with bands B02 and B04 with 1 s time lag, the
 428 uncertainty of U from the phase difference method for wavenumbers from 30 to 40

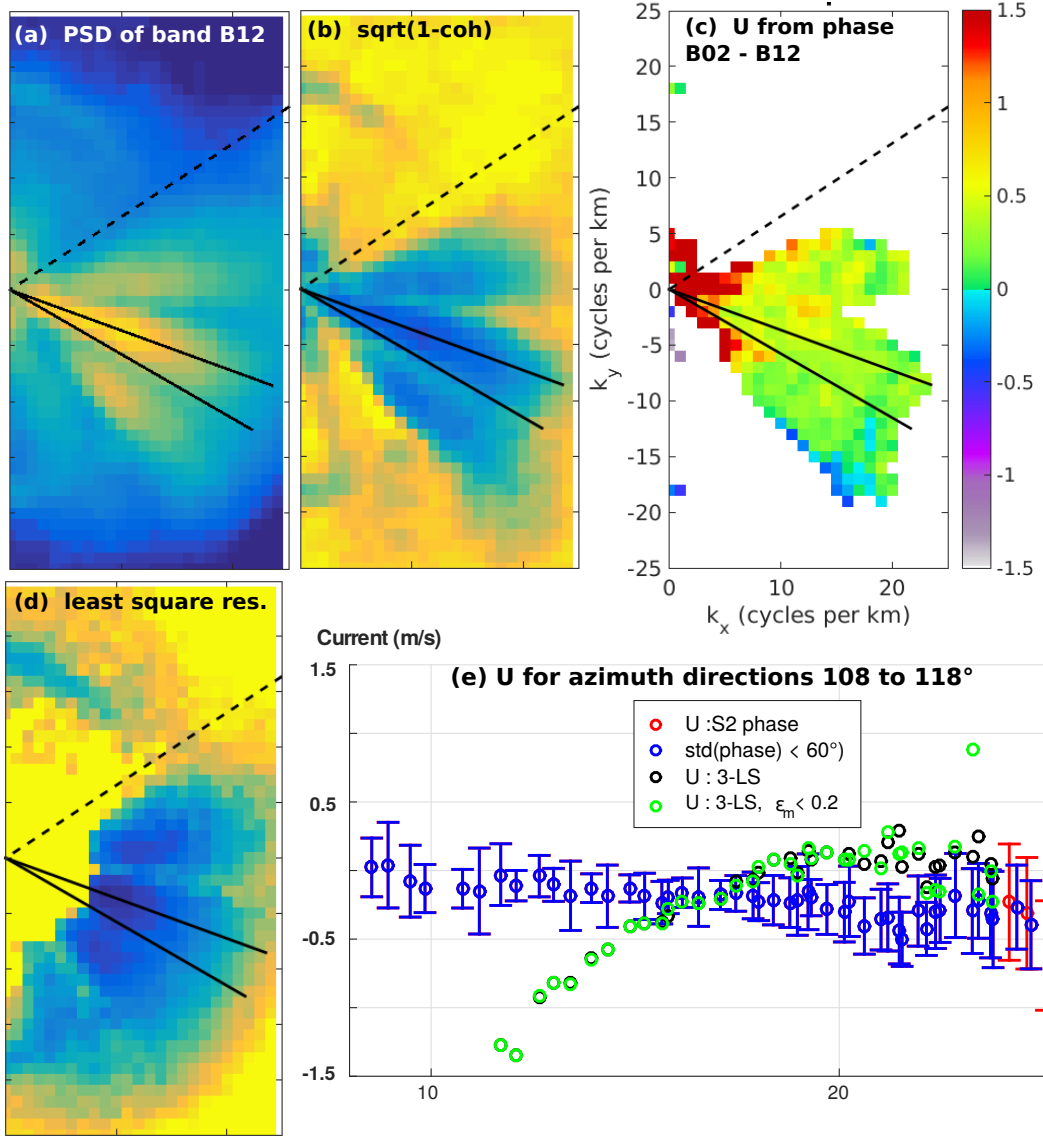


Figure 12. Example of results with a larger time lag of 2.1 s but coarser ($dx=20m$) using B12 and B02 bands. In order to better resolve the longer waves, the spectral analysis was done here with 1 km by 1 km tiles.

429 cpm is larger at 4.8 cm/s due to the opposing effects of a lower coherence and a
 430 larger number of spectral estimates.

431 **4 Discussion: consequences for surface current velocity and shear re-** 432 **trieval**

433 **4.1 Application to Sentinel 2**

434 From the consistency of the velocity estimates for all spectral components, and
 435 in the particular case of the image analysed in Fig. 2 and 11, we find that Sentinel 2
 436 imagery is capable of providing a velocity precision of the order of 5 cm/s for spectral
 437 ranges of 10 cycles per kilometer. These uncertainties are of the order of the differences

438 in the advection speed of the different spectral components due to a typical vertical
 439 current shear in the top 20 m of the ocean. Along the equator with differences of
 440 the order of 50 cm/s between can be found between 1 m and 15 m depth and these
 441 should be detectable by Sentinel-2. A probably more typical shear, from subtropical
 442 Atlantic measurements, is shown in Fig. 13 and measuring it requires detecting 3
 443 cm/s differences between $k = 20$ cpkm and $k = 40$ cpkm. Resolving this demands a
 444 reduction of the uncertainty by at least a factor 3, possibly obtained by averaging over
 445 at least 24 by 24 km.

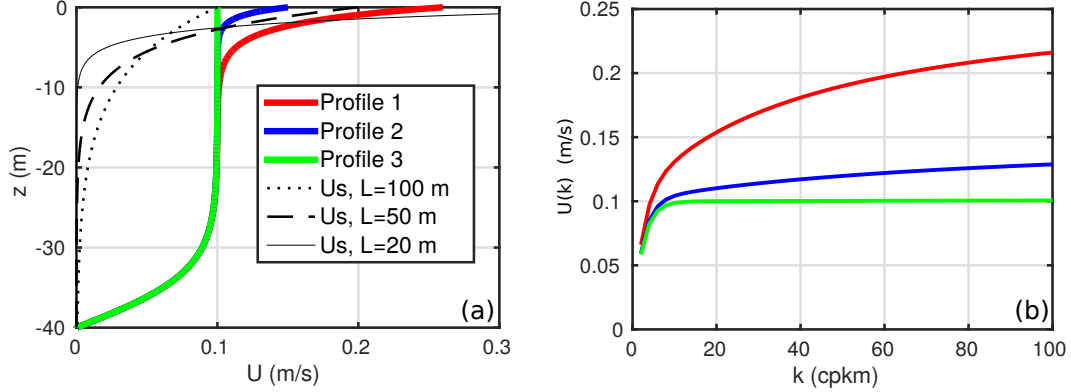


Figure 13. (a) Example of typical current profiles of summertime subtropical gyres. Profiles 1 and 2 correspond to figure 1, while profile 3 would be a hypothetical total current profile without Stokes drift. (b) Resulting variation of the effective current $U(k)$ as a function of the wavenumber.

446 At that level of accuracy, other phenomena may be involved, such as non-linear
 447 wave effects, that include both an advection of short waves by long waves (Weber &
 448 Barrick, 1977; Broche et al., 1983) which corresponds to a fraction of the Stokes drift
 449 (Ardhuin et al., 2009), and the presence of harmonics (i.e. Leckler et al., 2015). In
 450 order to test that latter effect we have made some simulations by replacing the linear
 451 wave model with the Choppy Wave Model (Nouguier et al., 2009), which is a first
 452 order Lagrangian theory. We use a current ($U_x = -1$ m/s, $U_y = 0$.) in our simulations.

Following (Yurovskaya et al., 2019), we estimate U_x and U_y by a least square fit to the measured phase differences after removing the linear wave dispersion,

$$\psi_a(k_x, k_y) = \left(\psi(k_x, k_y) - dt \sqrt{g \sqrt{k_x^2 + k_y^2}} \right) / dt \quad (9)$$

which is related to the current vector (U_x, U_y) by

$$\psi_a(k_x, k_y) = k_x U_x + k_y U_y + \varepsilon(k_x, k_y), \quad (10)$$

453 where ε is a small residual. We only keep the M spectral components with index m
 454 corresponding to one pair (k_x, k_y) such that $|k_m| > 10$ cpkm, $|k_m| < 40$ cpkm and
 455 with $\text{std}(\psi) < 60^\circ$. This gives a length M vector $Y = (\psi_{a,m})_{1 \leq m \leq M}$. We invert eq.
 456 (10) for all m to find the vector $X = (U_x, U_y)$ that gives the smallest sum of square
 457 residuals weighted by $1/\text{std}(\psi)^2$. The resulting uncertainty σ_U is the square root of
 458 the first term of the matrix $(A'CA)^{-1}$ where $A(m, 1) = k_{x,m}$, $A(m, 2) = k_{y,m}$ and C
 459 is the diagonal matrix such that $C(m, m) = 1/\text{std}(\psi_m)^2$ (Hogg et al., 2010).

In our case, we take as a reference $\sigma_{U,l} = 0.018$ m/s the uncertainty on retrieved U for the case of a linear MTF and linear surface. This uncertainty is not zero due

Table 1. Effect of nonlinearities and opposing waves on retrieved current

Simulation	U value	$\sigma_{u,Z}$
Linear Model	-0.974	0.000
Choppy Wave Model	-0.976	0.011
nonlinear MTF	-0.975	0.004
Opposing waves	-0.899	0.107

to all the processing steps: use sub-images, windows, etc. Presumably the effect of non-linearities or waves in opposing directions are independent from these processing effects and we estimate the excess uncertainty due to effect Z , as

$$\sigma_{U,Z} = \sqrt{\sigma_U^2 - \sigma_{U,l}^2}. \quad (11)$$

The retrieved current and excess uncertainty are reported in Table 1 for 4 different simulations. We find that the effects of non-linearities introduced by the Choppy Wave Model for wavelengths larger than 20 m and in the case considered here, are comparable to the effect of the non-linear MTF and 9 times smaller than the effect of waves in opposite directions. Possibly nonlinearity becomes more important when waves much shorter than $L = 20$ m are taken into account.

Also, waves are not homogeneous in space, with gradient driven by the horizontal shear of small scale currents (Arduin et al., 2017; Quilfen & Chapron, 2019; Villas Bôas et al., 2020). If the shorter waves correlate with currents in a way different from the longer waves, which can be the case at the smallest scales (Suzuki, 2019), what appears like a vertical shear in the difference of phase speed could be the effect of the horizontal shear. Detailed simulations of these effects will be needed to find the order of magnitude of horizontal shear contributions to the mean phase speed difference.

In general, the vertical shear of the current is a priori not sensitive to image co-registration errors because all wavelengths are affected by these errors in the same way, and the shear is associated by a difference in phase speed of the different wave components. We find that a 10 cm/s difference in phase speed between 50 m and 25 m wavelengths ($k=20$ cpkm and $k=40$ cpkm) should be detectable with Sentinel-2 using data from a 8 km by 8 km region of the ocean. Such a difference correspond to a fairly large current shear in the top 10 m of the ocean.

4.2 Beyond Sentinel 2: a possible STREAM-O instrument

Resolving weaker and more typical shears would require more sensitive measurements such as provided with larger time lags and higher spatial resolution. Fig. 13.b shows that extending the spectrum to 100 cpkm (10 m wavelengths) would double the difference in velocity that can be detected. Such capability will be available with the next generation Sentinel 2. Using these shorter components will probably require methods that are less sensitive to the presence of waves in opposite directions, such as the least square method proposed here.

Based on the results shown in Section 3, increasing time lags is probably the most important feature needed to obtain more accurate currents using both the phase difference or the least square methods, with or without waves in opposing directions. Due to data downlink constraints and cloud cover, optical monitoring of currents using wave dispersion cannot compete with the possible coverage given by radar systems (Arduin et al., 2019). Yet, optical imagery are uniquely capable of providing estimates

495 of vertical current shear, and may provide very useful data for reducing pointing errors.
 496 With these two goals in mind, the "ocean Surface Transport kinetic Energy, Air-sea
 497 fluxes and Mixing" (STREAM) concept combines a Ka-band Doppler scatterometer
 498 radar STREAM-R with a 1000 km wide radar swath, with an optical system STREAM-
 499 O that takes sequences of 5 ocean images at 5 m resolution with time lags of 1, 4, 9 and
 500 10 s, overlapping over a 10 km wide strip along the orbit. This concept was proposed
 501 for the 11th Earth Explorer of the European Space Agency.

502 In addition to the increased time lag, The STREAM-O design uses a push-frame
 503 acquisition system, instead of the push-broom of the MSI sensor on Sentinel 2. Namely,
 504 the raw data for one band consists of 2-D images with large overlaps instead of a single
 505 line. Such a feature makes on-board averaging possible, increasing the integration time
 506 to a value larger than several times the life time of specular points, i.e. 10 milliseconds
 507 or more. This is clearly not feasible for a pushbroom system in which the duration of
 508 the acquisition of each pixel is less than the pixel size (10 m) divided by the ground
 509 velocity (7 km/s), i.e. 1.4 ms. Future work is needed to understand the parameters
 510 that control the phase difference noise in optical imagery. It is possible that other
 511 parameters are relevant besides the number and life time of specular points. Also,
 512 the present paper considered images in the sun glint, but several useful applications
 513 (in particular for water depth retrieval) have been made with different observation
 514 geometries, with different noise characteristics.

515 5 Conclusions

516 In order to retrieve a surface current vector and current shear from observed
 517 wave dispersion it is necessary to obtain separate and robust estimates of the phase
 518 speed of different components of the wave spectrum, with different directions to obtain
 519 a current vector, and with different wavelengths that have different sensitivities to
 520 different depths.

521 Although the present work did not demonstrate a full solution method, we have
 522 highlighted difficulties associated to the retrieval of phase speed from a small number
 523 of ocean surface images using either a phase difference method or a least square fit-
 524 ting of the current velocity and the amplitude of waves in opposing directions. Both
 525 methods have complementary advantages and should probably be combined and mod-
 526 ified for further improvements. We particularly highlighted how the presence of waves
 527 in opposite directions cause an error in the phase difference method. In one specific
 528 case analyzed here, this is particularly a problem for retrieving phase speeds from
 529 waves with wavelengths shorter than 4 times the dominant wind sea. The least square
 530 method using 3 or more images is not sensitive to waves in opposing directions, but
 531 it provides relatively noisy estimates of the current velocity when applied to Sentinel
 532 2, due to the short time lags (about 1 s). As a result, the least square method may
 533 not provide much more useful additional information on the current velocity than the
 534 phase difference method. We also note that anomalously low coherence in image pairs
 535 may be an indication of the presence of waves in opposite directions, which may have
 536 application to the identification of strong microseism or microbarom sources.

537 Our simulations show that when applied to other sensors with lower image noise
 538 and/or larger time lags, the least square method may allow to use the shortest wave
 539 components that are more likely to be associated to high levels of energy propagating
 540 in opposing directions. We find that a 2 s time separation and the same pixel noise as
 541 Sentinel 2 should be sufficient to retrieve reliable phase speeds of shorter waves, all the
 542 way to the Nyquist wavelength. In that case it should be viable to reliably estimate the
 543 magnitude of waves in opposing directions as quantified by the opposition spectrum
 544 introduced in Section 2. Future work will be needed to refine and verify the error
 545 model for the two methods and their possible combination.

Appendix A Image simulator

The first 5 directional moments are converted to a 5-degree resolution directional frequency spectrum using the Maximum Entropy Method (Lygre & Krogstad, 1986). This spectrum is then interpolated onto a regular grid in (k_x, k_y) space to obtain power spectral densities of wave-induced surface elevation with a spectral resolution of 1/16000 cycles per meter, i.e. with a largest wavelength of 16 km, twice as large as the region analyzed. Drawing random phases for each spectral component, the wave power spectral density is used to define complex amplitudes that are inverse-Fourier transformed to generate 8 km square grids of the surface elevation and long wave slopes, $(s_x(x, y, t_i), s_y(x, y, t_i))$, with x and y regularly discretized at 10 m resolution, and t_i the discrete time sampling corresponding to the time of image acquisition.

The input to our image simulator are thus

- the wave spectrum $F(f, \theta)$ is transformed to $F(k_x, k_y)$ using linear dispersion with a maximum frequency $f \simeq 0.7$ Hz corresponding to a cut of wavelength of 3.2 m. This spectrum is then interpolated on a regular grid in (k_x, k_y) space, covering the range $[-k_N, k_N]$ for each dimension where k_N is the Nyquist frequency (i.e. corresponding to a 20 m wavelength when simulating 10 m resolution images). This avoids any aliasing.
- the direction of the dominant slopes φ_{mss} (which is generally close to the wind direction)
- the mean square slope in that direction mss_u and the mean square slope in the perpendicular cross-direction mss_c .
- the bistatic view angles β and φ_a for each image (see Figure 2 for a definition), which we assume spatially uniform as we are only representing a small piece of the ocean

Ideally a full wave spectrum including short gravity waves, e.g. such as parameterized by Elfouhaily et al. (1997) or extending the model range of WAVEWATCH III to short gravity waves, would also contain the required slope parameters (items 2 and 3 of the above list), but such spectra are not yet realistic enough.

The forward model described in Kudryavtsev et al. (2017a) is used to compute a mean luminance B_0 for a locally rough but flat surface, and the local luminance $B(x, y)$ from the same rough surface tilted by the long wave slopes. Detected luminance fluctuations are caused by the true luminance fluctuations caused by the finite number of specular points that contribute to the signal in each pixel (Longuet-Higgins, 1960).

The image pixel value is then taken as the nearest integer of a mean intensity $\langle I \rangle$ times $(1 + n_t)B/B_0$ where n_t is a random white noise of a amplitude N_t that parameterizes the "twinkle" of the sea surface.

The noise of the detector is treated as an additive noise n_d , represented as a Gaussian noise of standard deviation N_d . For each channel j which corresponds to a time t_j we have the pixel value

$$I_j(x, y) = \text{E}(\langle I \rangle_j B(x, y, t_j) / B_0 (1 + n_t)), \quad (\text{A1})$$

where the value $\text{E}(x)$ is the largest integer value that is less or equal to x . The quantization effect of rounding to an integer pixel value is not very relevant in the present paper with examples that have a relatively bright sea surface. In contrast, the twinkle noise has a very important influence on the estimation of the surface current, as discussed in Sections 2 and 3.

Appendix B Adaptation of 3-probe least squares method to an unknown current

Let us have A and B the complex amplitudes of the waves propagating in the φ direction and the opposite direction $\varphi + \pi$, and N is the number of measurements at times t_n . In the case $N = 3$, the system of equations for the 3 measured complex amplitudes F_1, F_2, F_3 at times $t_1 = 0, t_2, t_3$ is, for each spectral component (k, φ) , with U the current component in direction φ , $\sigma = \sqrt{gk}$,

$$A + B - F_1 = \varepsilon_1, \quad (\text{B1})$$

$$Ae^{-i(\sigma t_2 - kUt_2)} + Be^{+i(\sigma t_2 + kUt_2)} - F_2 = \varepsilon_2, \quad (\text{B2})$$

$$Ae^{-i(\sigma t_3 - kUt_3)} + Be^{+i(\sigma t_3 + kUt_3)} - F_3 = \varepsilon_3. \quad (\text{B3})$$

$$(\text{B4})$$

We look for the solution that minimizes the sum of the modulus of ε_n squared,

$$\sum_n |\varepsilon_n|^2 = \sum_n \left(Ae^{-i(\sigma t_n - kUt_n)} + Be^{+i(\sigma t_n + kUt_n)} - F_n \right) \left(\overline{A}e^{i(\sigma t_n - kUt_n)} + \overline{B}e^{-i(\sigma t_n + kUt_n)} - \overline{F}_n \right) \quad (\text{B5})$$

where the overbar corresponds to the complex conjugate. Taking derivatives with respect to the real and imaginary parts of A and B and taking derivative with respect to U gives, respectively,

$$\sum_n e^{-i(\sigma t_n - kUt_n)} \left(Ae^{-i(\sigma t_n - kUt_n)} + Be^{+i(\sigma t_n + kUt_n)} - F_n \right) = 0 \quad (\text{B6})$$

$$\sum_n e^{+i(\sigma t_n + kUt_n)} \left(Ae^{-i(\sigma t_n - kUt_n)} + Be^{+i(\sigma t_n + kUt_n)} - F_n \right) = 0 \quad (\text{B7})$$

$$\sum_n t_n \text{Im} \left[\left(Ae^{-i(\sigma t_n - kUt_n)} + Be^{+i(\sigma t_n + kUt_n)} \right) \left(Ae^{-i(\sigma t_n - kUt_n)} + Be^{+i(\sigma t_n + kUt_n)} - F_n \right) \right] = 0, \quad (\text{B8})$$

where $\text{Im}(X)$ is the imaginary part of X .

Using $t_1 = 0$, this can be re-arranged as

$$\alpha A + \beta B = \gamma \quad (\text{B9})$$

$$\beta A + \delta B = \gamma' \quad (\text{B10})$$

$$\begin{aligned} & \text{Im}[t_2 (\alpha_2 A + \beta_2 B) \cdot (\alpha_2 A + \beta_2 B - F_2) \\ & + t_3 (\alpha_3 A + \beta_3 B) \cdot (\alpha_3 A + \beta_3 B - F_3)] = 0 \end{aligned} \quad (\text{B11})$$

where we have defined

$$\alpha = \left[1 + e^{-i(2\sigma - 2kU)t_2} + e^{-i(2\sigma - 2kU)t_3} \right] \quad (\text{B12})$$

$$\beta = \left[1 + e^{i2kUt_2} + e^{i2kUt_3} \right] \quad (\text{B13})$$

$$\gamma = F_1 + F_2 e^{-i(\sigma - kU)t_2} + F_3 e^{-i(\sigma - kU)t_3} \quad (\text{B14})$$

$$\delta = \left[1 + e^{2i(\sigma + kU)t_2} + e^{2i(\sigma + kU)t_3} \right] \quad (\text{B15})$$

$$\gamma' = F_1 + F_2 e^{i(\sigma + kU)t_2} + F_3 e^{i(\sigma + kU)t_3} \quad (\text{B16})$$

$$\alpha_2 = e^{-i(\sigma - kU)t_2} \quad (\text{B17})$$

$$\beta_2 = e^{i(\sigma + kU)t_2} \quad (\text{B18})$$

$$\alpha_3 = e^{-i(\sigma - kU)t_3} \quad (\text{B19})$$

$$\beta_3 = e^{i(\sigma + kU)t_3} \quad (\text{B20})$$

We may eliminate A and B from the first 2 equations giving

$$A = (\gamma - \beta B) / \alpha, \quad (\text{B21})$$

and

$$B = (\gamma' - \gamma\beta/\alpha) / (\delta - \beta^2/\alpha). \quad (\text{B22})$$

601 replacing these expressions for A and B in eq. (B11) gives one equation for U ,

$$\begin{aligned} f(U, k, \sigma, F_1, F_2, F_3, t_2, t_3) = \text{Im} [& t_2 (\alpha_2 A + \beta_2 B) \times (\alpha_2 A + \beta_2 B - F_2) \\ & + t_3 (\alpha_3 A + \beta_3 B) \times (\alpha_3 A + \beta_3 B - F_3)] = 0. \end{aligned} \quad (\text{B23})$$

602 Finding the solution for $f = 0$ gives an estimate of the value of U . This operation
603 can be repeated for each Fourier transform (each tile) and each spectral component.
604 Different averaging procedures are discussed in Section 3. In particular we find that
605 the square root of the sum of $|\varepsilon_n|^2$ is linearly correlated to the error on U , in particular
606 when the phase differences are large. Finally, this approach is easily extended to more
607 than 3 images.

608 Acknowledgments

609 We acknowledge the use of Copernicus Sentinel 2 data, obtained from the Copernicus
610 Science Hub <https://scihub.copernicus.eu>, and buoy data were furnished by
611 the Coastal Data Information Program (CDIP), Integrative Oceanography Division,
612 operated by the Scripps Institution of Oceanography, under the sponsorship of the
613 U.S. Army Corps of Engineers and the California Department of Parks and Recreation
614 <https://doi.org/10.18437/C7WC72>. F.A. and M.A. were supported by CNES as
615 part of the SKIM preparation program and ANR grants for ISblue (ANR-17-EURE-
616 0015) and MIMOSA (ANR-14-CE01-0012), with additional support from the European
617 Space Agency, through the IASCO contract 4000129945/19/NL/FF/gp. M.Yu.
618 was supported by Ministry of Science and Education of the Russian Federation under
619 State Assignment No. 0555-2021-0004 and Russian Science Foundation through the
620 Project No. 21-47-00038. We thank Bertrand Chapron for fruitful discussions and two
621 anonymous reviewers that have helped make the manuscript much more readable.

622 References

- 623 Andrews, D. G., & McIntyre, M. E. (1978). On wave action and its relatives. *J.*
624 *Fluid Mech.*, *89*, 647–664. (Corrigendum: vol. 95, p. 796)
- 625 Ardhuin, F., Chapron, B., Collard, F., Smith, M., Stopa, J., Thomson, J., ...
626 Collins, C. O., III (2017). Measuring ocean waves in sea ice using
627 SAR imagery: A quasi-deterministic approach evaluated with Sentinel-
628 1 and in situ data. *Remote sensing of Environment*, *189*, 211–222. doi:
629 10.1016/j.rse.2016.11.024
- 630 Ardhuin, F., Chapron, B., Maes, C., Romeiser, R., Gommenginger, C., Cravatte, S.,
631 ... Bourassa, M. (2019). Satellite doppler observations for the motions of the
632 oceans. *Bull. Amer. Meteorol. Soc.*, *100*. doi: 10.1175/BAMS-D-19-0039.1
- 633 Ardhuin, F., Gualtieri, L., & Stutzmann, E. (2015). How ocean waves rock the
634 earth: two mechanisms explain seismic noise with periods 3 to 300 s. *Geophys.*
635 *Res. Lett.*, *42*, 765–772. doi: 10.1002/2014GL062782
- 636 Ardhuin, F., Marié, L., Rascle, N., Forget, P., & Roland, A. (2009). Observation and
637 estimation of Lagrangian, Stokes and Eulerian currents induced by wind and
638 waves at the sea surface. *J. Phys. Oceanogr.*, *39*(11), 2820–2838. Retrieved
639 from <http://journals.ametsoc.org/doi/pdf/10.1175/2009JPO4169.1> doi:
640 10.1175/2009JPO4169.1

- 641 Arduin, F., & Roland, A. (2012). Coastal wave reflection, directional spreading,
642 and seismo-acoustic noise sources. *J. Geophys. Res.*, *117*, C00J20. doi: 10
643 .1029/2011JC007832
- 644 Barrick, D. E. (1977). Extraction of wave parameters from measured HF radar sea-
645 echo Doppler spectra. *Radio Science*, *12*, 415–423.
- 646 Brekhovskikh, L. M., Goncharov, V. V., Kurteпов, V. M., & Naugolnykh, K. A.
647 (1973). The radiation of infrasound into the atmosphere by surface waves in
648 the ocean. *Izv. Atmos. Ocean. Phys.*, *9*, 899–907 (In the English translation,
649 511–515.).
- 650 Broche, P., de Maistre, J. C., & Forget, P. (1983). Mesure par radar décimétrique
651 cohérent des courants superficiels engendrés par le vent. *Oceanol. Acta*, *6*(1),
652 43–53.
- 653 Campana, J., Terrill, E. J., & Paolo, T. D. (2016). The development of an inversion
654 technique to extract vertical current profiles from X-band radar observations.
655 *J. Atmos. Ocean Technol.*, *33*, 2015–2028. doi: 10.1175/JTECH-D-15-0145.1
- 656 Cronin, M. F., Gentemann, C. L., Edson, J., Ueki, I., Bourassa, M., Brown, S.,
657 ... Zhang, D. (2019). Air-sea fluxes with a focus on heat and momentum.
658 *Frontiers in Marine Sci.*, *6*, 430.
- 659 De Carlo, M., Arduin, F., & Pichon, A. L. (2020). Atmospheric infrasound ra-
660 diation from ocean waves in finite depth: a unified generation theory and
661 application to radiation patterns. *Geophys. J. Int.*, *221*, 569–585. doi:
662 10.1093/gji/ggaa015
- 663 Drusch, M., Del Bello, U., Carlier, S., Colin, O., Fernandez, V., Gascon, F., ...
664 Bargellini, P. (2012). Sentinel-2: Esa’s optical high-resolution mission for gmes
665 operational services. *Remote sensing of Environment*, *120*, 25–36. (The Sen-
666 tinel Missions - New Opportunities for Science) doi: 10.1016/j.rse.2011.11.026
- 667 Elfouhaily, T., Chapron, B., Katsaros, K., & Vandemark, D. (1997). A unified di-
668 rectional spectrum for long and short wind-driven waves. *J. Geophys. Res.*,
669 *102*(C7), 15781–15796. doi: 10.1029/97jc00467
- 670 Elipot, S., Lumpkin, R., Perez, R. C., Lilly, J. M., Early, J. J., & Sykulski, A. M.
671 (2016). A global surface drifter data set at hourly resolution. *J. Geophys. Res.*,
672 *121*, 2937–2966. doi: 10.1002/2016JC011716
- 673 Farrell, W. E., & Munk, W. (2008). What do deep sea pressure fluctuations tell
674 about short surface waves? *Geophys. Res. Lett.*, *35*(7), L19605. doi: 10.1029/
675 2008GL035008
- 676 Fedele, F., Benetazzo, A., Gallego, G., Shih, P.-C., Yezzi, A., Barbariol, F., & Ard-
677 huin, F. (2013). Space-time measurements of oceanic sea states. *Ocean*
678 *Modelling*, *70*, 103–115. doi: 10.1016/j.ocemod.2013.01.001
- 679 Guimarães, P. V., Arduin, F., Bergamasco, F., Leckler, F., Filipot, J.-F., Shim, J.-
680 S., ... Benetazzo, A. (2020). A data set of sea surface stereo images to resolve
681 space-time wave fields. *Sci. Data*, *7*, 145. doi: 10.1038/s41597-020-0492-95
- 682 Hasselmann, K. (1963). A statistical analysis of the generation of microseisms. *Rev.*
683 *of Geophys.*, *1*(2), 177–210.
- 684 Hogg, D. W., Bovy, J., & Lang, D. (2010). Data analysis recipes: Fitting a model to
685 data. *ArXiv*, 1008.4686.
- 686 Kääh, A., Winsvold, S. H., Altena, B., Nuth, C., Nagler, T., & Wuite, J. (2016).
687 Glacier remote sensing using Sentinel-2. part I: Radiometric and geometric
688 performance, and application to ice velocity. *Radio Science*, *8*, 598. doi:
689 10.3390/rs807059
- 690 Kirincich, A. (2016). Remote sensing of the surface wind field over the coastal ocean
691 via direct calibration of HF radar backscatter power. *J. Atmos. Ocean Technol.*,
692 *33*(7), 1377–1392. doi: 10.1175/JTECH-D-15-0242.1
- 693 Kudryavtsev, V., Yurovskaya, M., Chapron, B., Collard, F., & Donlon, C. (2017a).
694 Sun glitter imagery of surface waves. part 1: Directional spectrum retrieval
695 and validation. *J. Geophys. Res.*, *122*. doi: 10.1002/2016JC012425

- 696 Kudryavtsev, V., Yurovskaya, M., Chapron, B., Collard, F., & Donlon, C. (2017b).
697 Sun glitter imagery of surface waves. part 2: Waves transformation on ocean
698 currents. *J. Geophys. Res.*, *122*. doi: 10.1002/2016JC012426
- 699 Laxague, N. J. M., Özgökmen, T. M., Haus, B. K., Novelli, G., Shcherbina, A.,
700 Sutherland, P., ... Molemaker, J. (2018). Observations of near-surface current
701 shear help describe oceanic oil and plastic transport. *Geophys. Res. Lett.*, *44*,
702 245–249. doi: 10.1002/2017GL075891
- 703 Lebedev, K., Yoshinari, H., Maximenko, N. A., & W., H. P. (2007). *Yomaha07: velocity data assessed from trajectories of argo floats at park-*
704 *ing level and at the sea surface* (Tech. Rep. No. 4). Int. Pac. Res.
705 Cent., Univ. Hawaii, Honolulu. Retrieved from [http://apdrc.soest](http://apdrc.soest.hawaii.edu/projects/yomaha/yomaha07/YoMaHa070612small.pdf)
706 [.hawaii.edu/projects/yomaha/yomaha07/YoMaHa070612small.pdf](http://apdrc.soest.hawaii.edu/projects/yomaha/yomaha07/YoMaHa070612small.pdf)
707 ([<http://apdrc.soest.hawaii.edu/projects/yomaha/yomaha07/YoMaHa070612small.pdf>])
708
- 709
- 710 Leckler, F., Ardhuin, F., Peureux, C., Benetazzo, A., Bergamasco, F., & Dulov,
711 V. (2015). Analysis and interpretation of frequency-wavenumber spectra
712 of young wind waves. *J. Phys. Oceanogr.*, *45*, 2484–2496. doi:
713 10.1175/JPO-D-14-0237.1
- 714 Longuet-Higgins, M. S. (1960). Reflection and refraction at a random moving sur-
715 face. II. number of specular points in a gaussian surface. *J. Opt. Soc. Am.*,
716 *50*(9), 845–850. doi: 10.1364/JOSA.50.000845
- 717 Lumpkin, R., Özgökmen, T., & Centurioni, L. (2017). Advances in the application
718 of surface drifters. *Annu. Rev. Mar. Sci.*, *9*, 6.1–6.23. doi: 10.1146/annurev-
719 -marine-010816-060641
- 720 Lygre, A., & Krogstad, H. E. (1986). Maximum entropy estimation of the direc-
721 tional distribution in ocean wave spectra. *J. Phys. Oceanogr.*, *16*, 2,052–2,060.
- 722 Mansard, E. P. D., & Funke, E. R. (1980). The measurement of incident and re-
723 flected spectra using a least squares method. In *Proceedings of international*
724 *conference on coastal engineering* (Vol. 1). doi: 10.9753/icce.v17.8
- 725 Marié, L., Collard, F., Noguier, F., Pineau-Guillou, L., Hauser, D., Boy, F., ...
726 Ardhuin, F. (2020). Measuring ocean surface velocities with the kuros airborne
727 near-nadir doppler radar: a multi-scale analysis in preparation of the skim
728 mission. *Ocean Sci.*, *16*, 13991429. doi: 10.5194/os-16-1399-2020
- 729 Maximenko, N., Corradi, P., Law, K. L., Sebille, E. V., Garaba, S. P., Lampitt,
730 R. S., ... Wilcox, C. (2019). Toward the integrated marine debris observing
731 system. *Frontiers in Marine Sci.*, *6*, 447. doi: 10.3389/fmars.2019.00447
- 732 Niiler, P. P., & Paduan, J. D. (1995). Wind-driven motions in the Northeast Pacific
733 as measured by Lagrangian drifters. *J. Phys. Oceanogr.*, *25*(11), 2819–2930.
734 Retrieved from [http://ams.allenpress.com/archive/1520-0485/25/11/](http://ams.allenpress.com/archive/1520-0485/25/11/pdf/i1520-0485-25-11-2819)
735 [pdf/i1520-0485-25-11-2819](http://ams.allenpress.com/archive/1520-0485/25/11/pdf/i1520-0485-25-11-2819)
- 736 Noguier, F., Guérin, C.-A., & Chapron, B. (2009). “choppy wave” model
737 for nonlinear gravity waves. *J. Geophys. Res.*, *114*(C09), C09012. doi:
738 10.1029/2008JC004984
- 739 Novelli, G., Guigand, C. M., Cousin, C., Ryan, E. H., Laxague, N. J. M., Dai, H.,
740 ... Özgökmen, T. M. (2017). A biodegradable surface drifter for ocean sam-
741 pling on a massive scale. *J. Atmos. Ocean Technol.*, *34*, 2509–2532. doi:
742 10.1175/JTECH-D-17-0055.1
- 743 Peureux, C., Benetazzo, A., & Ardhuin, F. (2018). Note on the directional proper-
744 ties of meter-scale gravity waves. *Ocean Science*, *14*, 41–52. doi: 10.5194/os-14-
745 -41-2018
- 746 Quilfen, Y., & Chapron, B. (2019). Ocean surface wave-current signatures from
747 satellite altimeter measurements. *Geophys. Res. Lett.*, *216*, 253-261. doi: 10
748 .1029/2018GL081029
- 749 Rio, M.-H., Mulet, S., & Picot, N. (2014). Beyond GOCE for the ocean circulation
750 estimate: Synergetic use of altimetry, gravimetry, and in situ data provides

- 751 new insight into geostrophic and Ekman currents. *Geophys. Res. Lett.*, *41*,
752 8918–8925. doi: 10.1002/2014GL061773
- 753 Rodríguez, E., Wineteer, A., Perkovic-Martin, D., Gál, T., Stiles, B. W., Ni-
754 amsuwan, N., & Monje, R. R. (2018). Estimating ocean vector winds and
755 currents using a Ka-band pencil-beam doppler scatterometer. *Remote Sensing*,
756 *4*, 576. doi: 10.3390/rs10040576
- 757 Stewart, R. H., & Joy, J. W. (1974). HF radio measurements of surface currents.
758 *Deep Sea Res.*, *21*, 1039–1049.
- 759 Suzuki, N. (2019). On the physical mechanisms of the two-way coupling between
760 a surface wave field and a circulation consisting of a roll and streak. *J. Fluid*
761 *Mech.*, *881*, 906–950. doi: 10.1017/jfm.2019.752
- 762 Teague, C. C., Vesecky, J. F., & Hallock, Z. R. (2001). A comparison of multifre-
763 quency HF radar and ADCP measurements of near-surface currents during
764 COPE-3. *IEEE J. Oceanic Eng.*, *26*(3), 399–405.
- 765 Tyler, G. L., Teague, C. C., Stewart, R. H., Peterson, A. M., Munk, W. H., & Joy,
766 J. W. (1974). Wave directional spectra from synthetic aperture observations of
767 radio scatter. *Deep Sea Res.*, *21*, 989–1016.
- 768 Villas Bôas, A. B., Cornuelle, B. D., Mazloff, M. R., Gille, S. T., & Ardhuin, F.
769 (2020). Wave-current interactions at meso and submesoscales: Insights
770 from idealized numerical simulations. *J. Phys. Oceanogr.*, *in press*. doi:
771 10.1002/2016JC012413
- 772 Weber, B. L., & Barrick, D. E. (1977). On the nonlinear theory for gravity waves
773 on the ocean’s surface. Part I: Derivations. *J. Phys. Oceanogr.*, *7*, 3–10. Re-
774 trieved from [http://ams.allenpress.com/archive/1520-0485/7/1/pdf/](http://ams.allenpress.com/archive/1520-0485/7/1/pdf/i1520-0485-7-1-3.pdf)
775 [i1520-0485-7-1-3.pdf](http://ams.allenpress.com/archive/1520-0485/7-1-3.pdf)
- 776 Wunsch, C., & Ferrari, R. (2009). Ocean circulation kinetic energy: reservoirs,
777 sources, and sinks. *Annu. Rev. Fluid Mech.*, *41*, 253–282. doi: 10.1146/
778 annurev.fluid.40.111406.1021
- 779 Young, I. R., Rosenthal, W., & Ziemer, F. (1985). A three-dimensional analysis of
780 marine radar images for the determination of ocean wave directionality and
781 surface currents. *J. Geophys. Res.*, *90*, 1049–1059.
- 782 Yurovskaya, M., Kudryavtsev, V., Chapron, B., & Collard, F. (2019). Ocean surface
783 current retrieval from space: The sentinel-2 multispectral capabilities. *Remote*
784 *sensing of Environment*, *234*, 111468. doi: 10.1016/j.rse.2019.111468
- 785 Zelt, J. A., & Skjelbreia, J. E. (1993). Estimating incident and reflected wave fields
786 using an arbitrary number of wave gauges. In *Proceedings of 1992 international*
787 *conference on coastal engineering* (Vol. 1). doi: 10.1061/9780872629332.058